

# Effect of Post-deformation Annealing Treatment on the Microstructural Evolution of a Cold-Worked Corrosion-Resistant Superalloy (CRSA) Steel

A. Mirzaei, A. Zarei-Hanzaki, A. Mohamadizadeh, and Y.C. Lin

(Submitted June 24, 2017; in revised form September 20, 2017; published online February 5, 2018)

The post-deformation annealing treatments of a commercial cold-worked corrosion-resistant superalloy steel (Sanicro 28 steel) were carried out at different temperatures in the range of 900–1100 °C for different holding durations of 5, 10, and 15 min. The effects of post-deformation annealing time and temperature on the microstructural evolution and subsequent mechanical properties of the processed Sanicro 28 steel were investigated. The observations indicated that twin–twin hardening in cold deformation condition mainly correlates with abundant nucleation of mechanical twins in multiple directions resulting in considerable strain hardening behavior. Microstructural investigations showed that the static recrystallization takes place after isothermal holding at 900 °C for 5 min. Increasing the annealing temperature from 900 to 1050 °C leads to recrystallization development and grain refinement in the as-recrystallized state. In addition, an increase in annealing duration from 5 to 15 min leads to subgrain coarsening and subsequently larger recrystallized grains size. The occurrence of large proportion of the grain refinement, which is achieved in the first annealing stage at 1050 °C after 5 min, is considered as the main factor for the maximum elongation at this stage.

**Keywords** austenitic stainless steel, mechanical twin, static recrystallization, work hardening

## 1. Introduction

The corrosion-resistant superalloy (CRSA) steels with high contents of molybdenum, chromium, nickel, nitrogen and manganese are the most frequently used pipeline alloys in oil and gas transferring industries due to their remarkable physico-chemical, mechanical and corrosion-resistant characteristics (Ref 1–3). It is shown that the intrinsic properties of corrosion-resistant superalloys can be further improved through thermo-mechanical processing (TMP), which can take advantages of the corresponding microstructural evolutions (Ref 4).

In practice, the thermomechanical processing (TMP) of CRSA steels includes several rolling stages, either cold or hot, to shape the ingots into steel plates, considering the different combinations of thermal and mechanical treatment routes by which the final mechanical properties of the alloy can be controlled (Ref 2, 5–8). However, it is well known that the optimum mechanical properties of CRSA steels can be achieved simply through cold working followed by annealing treatment (Ref 9). The cold working step is usually considered as the shaping stage, while the annealing is an essential step to

relieve the stress and to generate the desired microstructure (Ref 10, 11).

In general, the microstructural evolution during the post-deformation heat treatment is dictated by the state of deformed matrix (including the amount of deformation stored energy) and the annealing parameters, i.e., temperature and holding time (Ref 12). From the metallurgical point of view, the accumulation of strain energy during cold working provides the driving force for the activation of different microstructural evolution mechanisms (Ref 8, 13). For instance, the occurrence of static recrystallization during thermal processing or inter-pass annealing may result in significant grain refinement. The statically recrystallized microstructures usually exhibit great combination of strength and ductility mainly due to the effective of grain refinement and newly formed dislocation-free grains, respectively (Ref 14, 15). The process of grains nucleation and growth is mainly accompanied by the long-range grain boundaries migration, which may consume the strain-hardened microstructure (Ref 16). These new grains are the result of static recrystallization through activating different mechanisms during annealing process such as gradual subgrain growth (Ref 17). In the latter mechanism, the sub-boundary misorientations are progressively increased until all the low-angle boundaries are transformed into the high-angle grain boundaries (Ref 18–20). During annealing, the microstructure is characterized by a mixture of increasing amounts of recrystallized grains and decreasing amounts of strain-hardened grains. The latter is related to the barriers facing the dislocation movement such as twin boundaries (Ref 21). The obstructing effect of mechanical twins which is related to the low stacking fault energy (SFE), on the motion of dislocations slip, is believed to be the main characteristic of the high work hardening potential alloys. In the most low-SFE alloys, the interaction of slip and twinning with the preexisted grain boundaries and prior twins in the microstructure introduces another complex component to the

A. Mirzaei, A. Zarei-Hanzaki, and A. Mohamadizadeh, The Complex Laboratory of Hot Deformation and Thermomechanical Processing of High Performance Engineering Materials, School of Metallurgy and Materials Engineering, College of Engineering, University of Tehran, Tehran, Iran; and Y.C. Lin, School of Mechanical and Electrical Engineering, Central South University, Changsha 410083, China. Contact e-mail: zareih@ut.ac.ir.

work hardening sensitivity, which includes back stress and accommodation effects at twin–grain boundary interfaces (Ref 22–25). Consequently, the generation and rearrangement of dislocation and twins during cold deformation result in additional strengthening behavior in the alloys. It is well reported that the work hardening rate increases when a large amount of twin–twin interactions occurs in the low-SFE alloy (Ref 26, 27). It is shown that the density and frequency of twinings increase by increasing the amount of strain and the stress (i.e., the alloy strength) by twin–twin interaction. Therefore, a cold-worked metal is in a state with a higher energy and therefore thermodynamically unstable (Ref 28, 29). In order to increase the microstructural stability and simultaneously generate the desirable combinations of mechanical properties, the predetermined post-deformation annealing treatment is necessitated. In fact, the precise control of post-deformation annealing treatments affects the final mechanical properties by: (1) decreasing the defect/dislocation density in the cold-worked material and (2) controlling the final microstructure in terms of grain size and morphology (Ref 30).

Despite the fact that many applied researches have been devoted on the dynamic restoration characterization of Sanicro 28 corrosion-resistant superalloy (CRSA) and considering that the alloy is strategically important and has great industrial applications (Ref 2, 6, 31), there are few studies focusing on the microstructural design through static restoration phenomena in this CRSA (Ref 9, 28, 32, 33). Moreover, the occurrence of twin–twin interaction during cold working of Sanicro 28 steel and evaluating the work hardening behavior has not been investigated. So, it is necessitated to understand the microstructure evolution and concurrent effect on the mechanical properties of a cold-worked and isochronally annealed Sanicro 28 austenitic stainless steel. Accordingly, in the present work, the effect of twin–twin interaction during work hardening and the static softening during post-annealing treatment on mechanical properties of Sanicro 28 corrosion-resistant superalloy (CRSA) with respect to microstructure characteristics are presented.

## 2. Experimental Procedure

The investigated Sanicro 28 steel was received in as-radial forged condition with the chemical composition given in Table 1. To eliminate any chemical and microstructural inhomogeneity, the alloy was homogenized at 1150 °C for 45 min. Cylindrical specimens were machined from the homogenized material with a length-to-diameter ratio of 1.5 ( $\Phi 10$  mm  $\times$  H15 mm) and subjected to uniaxial cold compression test. The tests were carried out using an Instron 4208 universal testing machine at the strain rate of  $0.1 \text{ s}^{-1}$  up to the true (logarithmic) strain of 0.7 in accordance with ASTM E209 standard. The variations of stress and strain were monitored continuously by a personal computer equipped with an automatic data acquisition system. A high-accuracy interface load cell (model: SSM-DJM-20 KN) with the capability of measuring the load forces down

to 0.1 kg was employed to record the load values. A set of interruption tests was executed at the strain rate of  $0.1 \text{ s}^{-1}$  to investigate the effect of strain on the microstructural evolution. The cold-deformed specimens were then subjected to a predetermined set of annealing treatment at 900, 1000, 1050, and 1100 °C for 5, 10, and 15 min. Each annealing cycle was followed by immediate water quenching to preserve the microstructure. The applied thermomechanical processing cycles are shown schematically in Fig. 1.

The specimens for microstructural observations were cut parallel to their longitudinal section. For all the samples, the center of the rectangular cross section was considered for representative metallographic observations. The selected section of the thermomechanically processed specimens was then mounted using cold curing resin and prepared through conventional metallography techniques. In order to reveal the microstructural features, the specimens were electro-polished and then etched in a 3:2:3 mixture of HCl, HNO<sub>3</sub> and H<sub>2</sub>O solution. X-ray diffraction (XRD) analysis was also employed to assure obtaining a single-phase austenitic structure and identify the absence of martensitic structure in the cold-worked specimens. For these tests, a high-resolution x-ray diffractometer (model Philips X'pert, Netherlands) with a rotating copper anode (Cu K $\alpha$ 1) radiation (wavelength,  $\lambda$  1.5406 Å) was employed.

The room temperature mechanical properties of the processed material were evaluated using the shear punch tests (SPT) with a  $\phi 3$ -mm cylindrical punch and a clearance distance of 0.04 mm. The SPT specimens were prepared by cutting the processed specimens into sections with an approximate thickness of  $300 \pm 15 \mu\text{m}$  via electro-discharge machine. In order to assure a sufficient technical accuracy in obtained data, the SPT was repeated three times for each condition. The tests were performed at the room temperature with the constant crosshead speed of  $0.2 \text{ mm min}^{-1}$ . The shear elongation was then

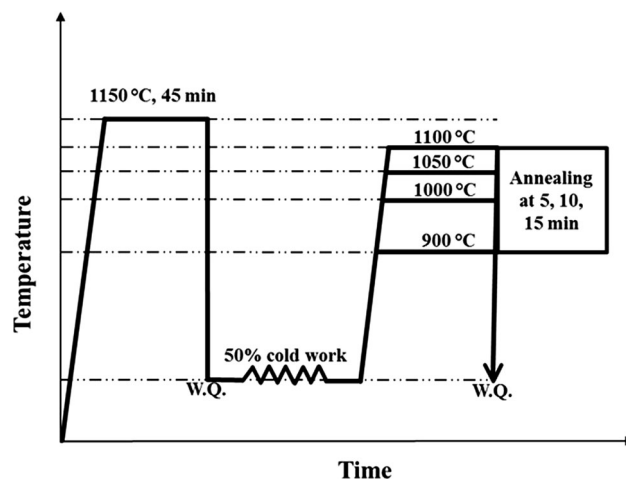


Fig. 1 Schematic representation of the applied thermomechanical processing cycles

Table 1 Chemical composition of the experimental steel (wt.%)

| C     | Mn   | Si   | Cr    | Ni    | P     | S       | Mo   | Cu   | Fe   |
|-------|------|------|-------|-------|-------|---------|------|------|------|
| 0.033 | 0.83 | 0.48 | 25.84 | 29.88 | 0.027 | < 0.001 | 3.06 | 0.61 | Base |

calculated from SPT data by employing the following empirical equation (Ref 34, 35):

$$\text{Elongation} = D/t \quad (\text{Eq 1})$$

where  $D$  is the difference of displacement at failure and  $t$  is the specimen thickness.

### 3. Results and Discussion

#### 3.1 The State of Cold Deformation Behavior

Figure 2(a) shows the initial microstructure of the experimental alloy after solution annealing prior to deformation. It represents a typical austenitic microstructure with the initial grain size of 132  $\mu\text{m}$ , which was measured by linear intercept method including quite a few annealing twins. The corresponding x-ray diffraction pattern (Fig. 2b) also confirms that the steel is fully austenitic.

The typical flow curve of the experimental CRSA steel obtained from the room temperature compression test at the strain rate of  $0.1 \text{ s}^{-1}$  up to the logarithmic strain of 0.7 is shown in Fig. 3(a). It can be seen that the material yields at a true compressive stress of about 300 MPa and undergoes a continuous strain hardening behavior up to 900 MPa at the

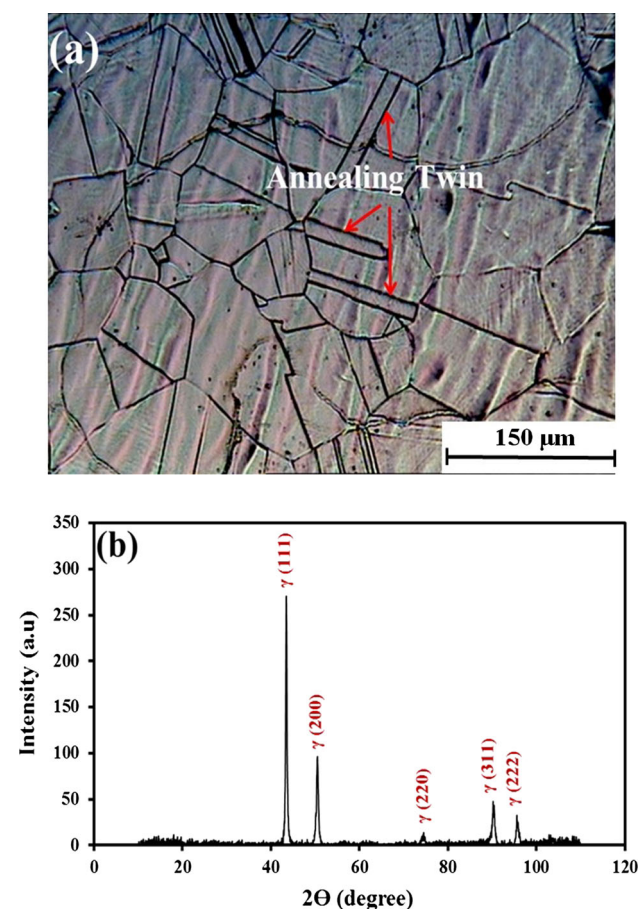


**Fig. 2** (a) Initial microstructure, and (b) the XRD pattern of the experimental CRSA steel in as-annealed condition

true strain of 0.7. The variation of strain hardening rate ( $\theta = \partial\sigma/\partial\epsilon$ ) is calculated and plotted versus the true strain in Fig. 3(b). As is seen, the variation of work hardening rate can be classified into three linear stages (Fig. 3b inner image). In the first hardening regime, stage A, the hardening rate is started to decrease from 0.02 to 0.21 true strains. Stage A is followed by another drop in strain hardening rate which is observed at higher strain levels from 0.21 to 0.4 true strains (stage B). At stage B, the strain hardening rate is decreased more rapidly. After the true strain of 0.4 is reached (stage C), the reduction speed of work hardening rate is lowered compared to stage B. According to previous studies, the deformation twins play a dominant role in the strain hardening response of low stacking fault energy (SFE) metals and metallic alloys (Ref 36). In the present study, the effect of deformation twinning on strain hardening behavior is discussed under the following subtitles:

#### i. Low strain regime (stage A)

The decrease in work hardening rate at stage A is usually attributed to the twin formation which may act as a dislocation barrier (Ref 37). It is well established that the annealing twin/austenite interfaces are potential sites for the nucleation and growth of mechanical twins (Ref 13). In addition, there is a critical resolved shear stress for activating mechanical twinning

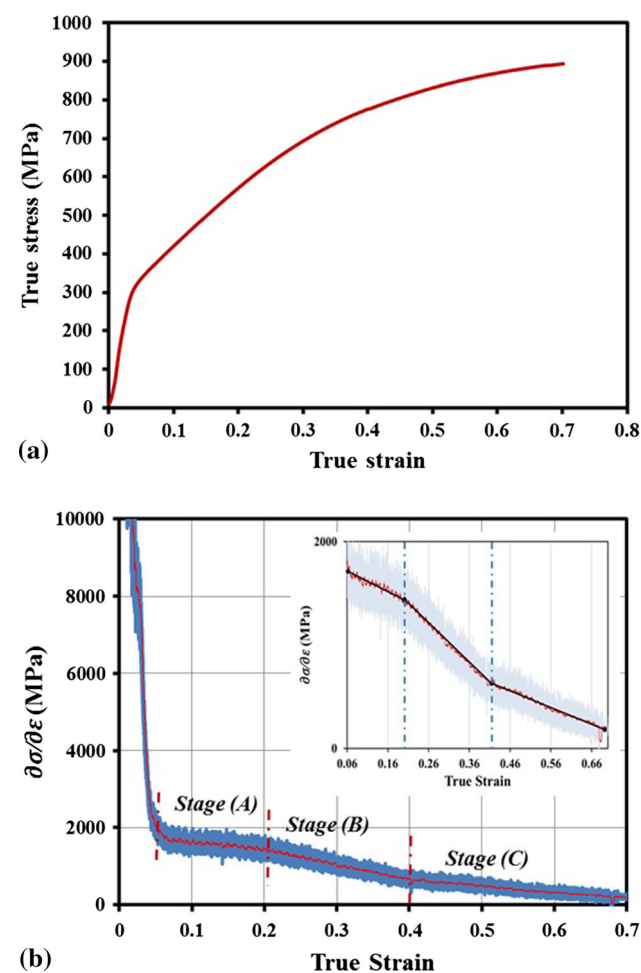


**Fig. 3** (a) Cold compression true stress–true (logarithmic) strain curve obtained under strain rate of  $0.1 \text{ s}^{-1}$ , (b) the variation of work hardening rate with true (logarithmic) strain



in each twinning system. Where the resolved shear stress on the twinning plane in the twinning direction reaches its critical value, the formation of new twins may occur as is observed in Fig. 4(a). It is assumed that the primary twinning may divide the original austenite grains into submicron regions, thereby playing an important role in restricting the dislocation movement during the further plastic deformation. The twins would lead to a local stress concentration. Therefore, a higher rate of strain hardening can be observed at stage A. This is the reason why the formation of mechanical twins can prevent the typical decrement in the rate of work hardening at early stages of deformation.

## ii. Medium strain regime (stage B)

As shown in Fig. 3(b), the work hardening rate decreases more rapidly during deformation at stage B. The most probable hypothesis is that the stage B occurs where there is a drop in the rate of primary twin formation. This experimental result may then call for a new explanation, since very few models are available in the literature to explain the decreasing rate of twin formation. Therefore, the following model based on our observations of the microstructural evolution (Fig. 4b) can be proposed in the present study. In low-SFE materials (apart from twin formation), the strain is found to be inherently nonhomogeneous at the grain scale (both within the grain and between the grains) (Ref 38). Consequently, significant misorientations may arise within grains even at moderate strains. According to the relevant microstructure (Fig. 4b), the curvatures in twins would be a clear indication of such in-grain misorientations, which has been resulted from the strain inhomogeneity within

the grains. As it is well known, the higher stresses are required for the nucleation of deformation twins in smaller grains compared to that of larger ones (Ref 39, 40). Hence, it is expected that the development of in-grain misorientations caused by inhomogeneous strain in the grain would significantly impede the formation of new deformation twins within the grains. This effect can be best justified from the data presented by Remy (Ref 41).

## iii. Large strain regions (stage C)

In accordance with Fig. 4(c), at logarithmic strains between 0.4 and 0.7 (stage C), having multiple twin directions within annealing twins and grains would inevitably lead to the formation of several parallel twin bands and the mutual intersection of mechanical twins in the grains. Therefore, the twin–twin interactions would contribute to an additional strengthening during the further twin formation at relatively higher amounts of deformation (Ref 26, 42). From the enlarged image in Fig. 4(d), it is noticeable that the intersection of the twins would form at the interface of the annealing twin/austenite region. The occurrence of twin–twin interactions in fcc low stacking fault energy alloys (such as Co33Ni, Fe-20Mn-4Cr-0.5C and Co-Fe alloys) have been widely investigated (Ref 27, 43, 44). The corresponding findings show that the strain hardening could be affected where a large amount of twin–twin interactions followed in these alloys. As is seen in Fig. 5(a), the twin–twin interactions at the true strain of 0.7 are more clearly observed.

In the present study, XRD patterns reveal an austenite single phase without martensitic or ferrite transformation during the

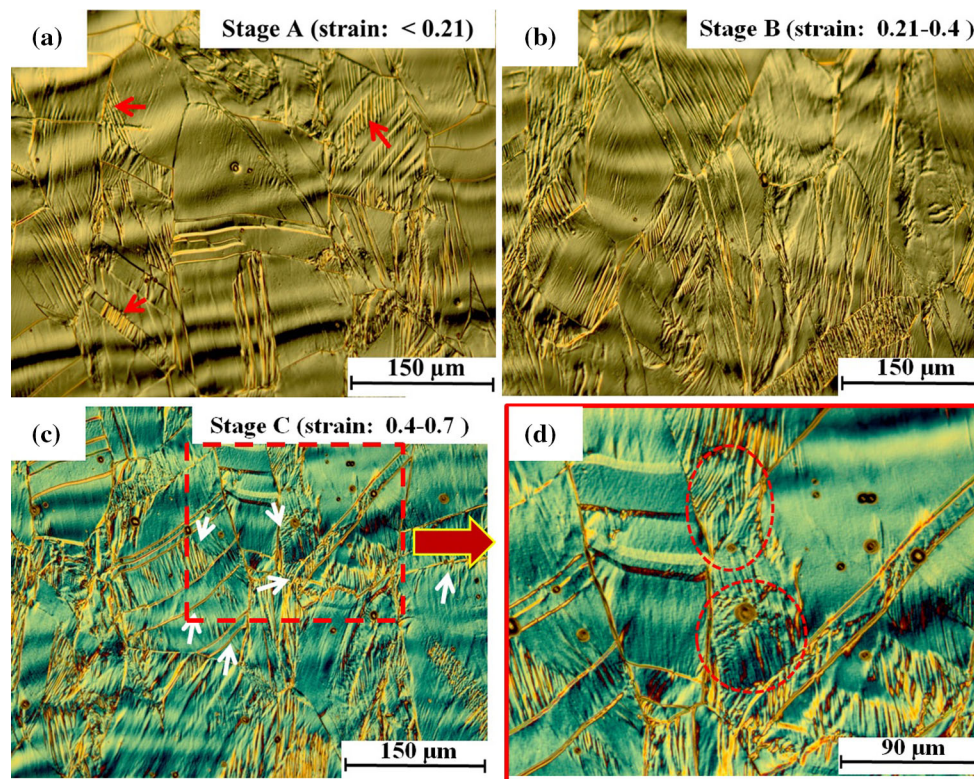


**Fig. 4** Microstructures of the experimental CRSA steel after interrupted compression tests at 25 °C: (a) after straining to 0.2, the initiation of mechanical twinning is seen, (b) after straining to 0.4, indicating the deformation twins, (c) the mechanical twin intersections are seen, after straining to 0.7, and (d) the enlarged image of mechanical twin interactions in stage C

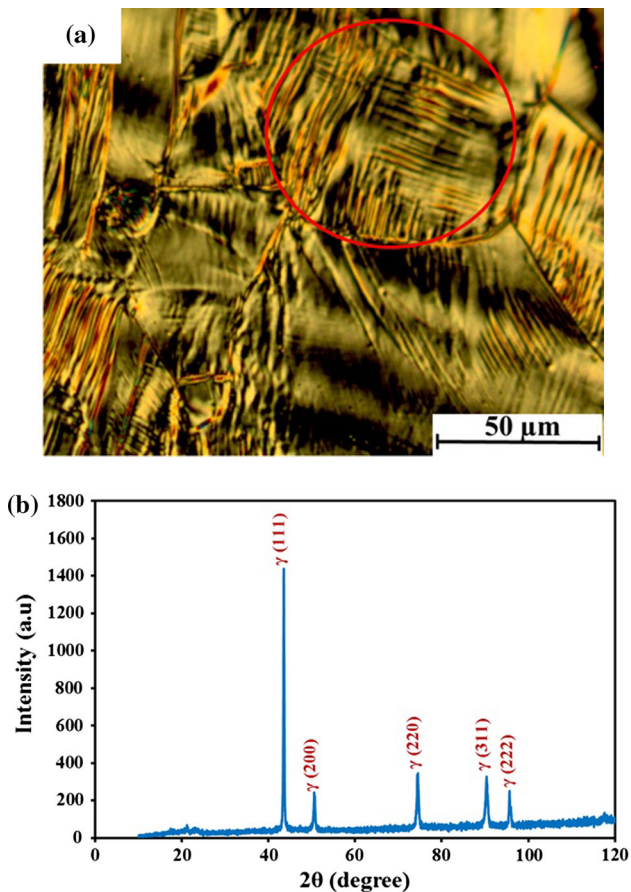


**Fig. 5** (a) Twin–twin interaction and (b) the XRD patterns of the corresponding specimen after straining to 0.7 (true strain)

cold work process. This can be taken as a proof for the fact that mechanical twinning is the solely and one of the most important mechanisms which is more likely to appear in the ambient temperature for the experimental alloy (Fig. 5b).

### 3.2 Microstructural Characterization After Annealing Treatment

In the second part of the present work, the effect of annealing conditions on the static recrystallization (SRX) behavior of the cold-deformed structure of the experimental alloy was studied by heating and holding some samples at different temperatures for various durations. It is important to note that a special attention is devoted on the role of twins on recrystallization behavior of the CRSA steel. The microstructural evolution of the cold-worked specimens after isothermally annealed at 900 and 1000 °C for 5, 10 and 15 min is illustrated in Fig. 6 and 7 respectively. As is seen, the recrystallized grains are emerged at the grain boundaries especially at the junctions of deformed grains in the specimen annealed at 900 and 1000 °C. It is well known that the strain energy of cold forming is highly accumulated at the preexisting high-angle boundaries (Ref 45). The deformation stored energy is a great source of driving force for providing preferential nucleation sites for static recrystallization (SRX). As a result, intergranular formation of new grains at the onset of SRX is expectable. In the

present study, an additional driving force for SRX can be provided due to the presence of twinning boundaries inside the grains. As is clearly observed, the recrystallization proceeds through the formation of a necklace type structure where the new grains are formed at the initial grain boundaries (Fig. 6 and 7). Besides, under such deformation condition, some austenite grains have remained in their original condition, which highlights the inhomogeneous evolution of the recrystallization process (shown in Fig. 6a and 7a). The reason for such inhomogeneous evolution is attributed to the inhomogeneity of deformation during cold working. In fact, the grain boundaries and triple junctions are more prone to the deformation stored energy because of the required compatibility strain to accommodate an incongruent shape change of grains at their common grain boundaries. This makes them particularly potential nucleation sites of SRX (Ref 46, 47). With respect to a non-uniform distribution of deformation stored energy within the microstructure, the nucleation first begins in the areas with the relatively highest stored energy and proceeds progressively toward the less energetic sites as the holding time and temperature are increased. For a better comparison, the obtained recrystallized grain size and the values of the volume fraction of recrystallized grains in the case of various times and temperatures for the annealed specimens are shown in Fig. 8. The fraction of the recrystallized grains is gradually increased with increasing annealing temperature and holding time. As is seen, the volume fraction of recrystallized grains increases from 25 to 36% when the holding time is increased from 5 to 15 min at 900 °C. Nevertheless, the relationship between holding time and the recrystallized grain size has insignificant alteration at 900 °C. As is expected, an increase in annealing temperature from 900 to 1000 °C leads to an increase in the recrystallized volume fraction and grain size regardless of holding time. Furthermore, annealing for 5-15 min leads to an increase in the volume fraction of recrystallized grains from 38 to 52% at 1000 °C. The distribution and the morphology of recrystallized grains are more uniform and equiaxed as the annealing time is increased at 1000 °C.

The corresponding microstructures of annealed specimens at 1050 and 1100 °C for 5, 10 and 15 min are shown in Fig. 9 and 10, respectively. As it can be seen, the microstructure is completely transformed to a fully recrystallized one in the temperature range from 1050 to 1100 °C as it consists of uniformly distributed fine grains. According to Fig. 8 and 9, annealing for 5 min at 1050 °C leads to the smallest grain size of about 6.7 μm among the studied experimental conditions. Annealing for longer holding time, i.e., 10 and 15 min results in dramatic grain growth of recrystallized grains (Fig. 8b) from 6.7 to 10.1 μm and 16.7 μm for 10 and 15 min annealing durations, respectively. The microstructural evolution during the annealing process at 1100 °C (Fig. 10) reveals that the annealing temperature has a profound effect on recrystallization which means the larger grains ensues from the higher temperature at these conditions. In fact, while SRX is the microstructural mechanism, rapid grain growth at 1100 °C results in a considerable coarsening of the initial fine-grained structure. As is shown in Fig. 8(b), by increasing temperature up to 1100 °C, the grain sizes are almost multiplied by 1.5 compared to those in 1050 °C. However, the longer annealing duration at 1150 °C, i.e., 10 and 15 min, is not seemed to cause a noticeable change in recrystallized grain size compared to the shorter annealing period of 5 min.



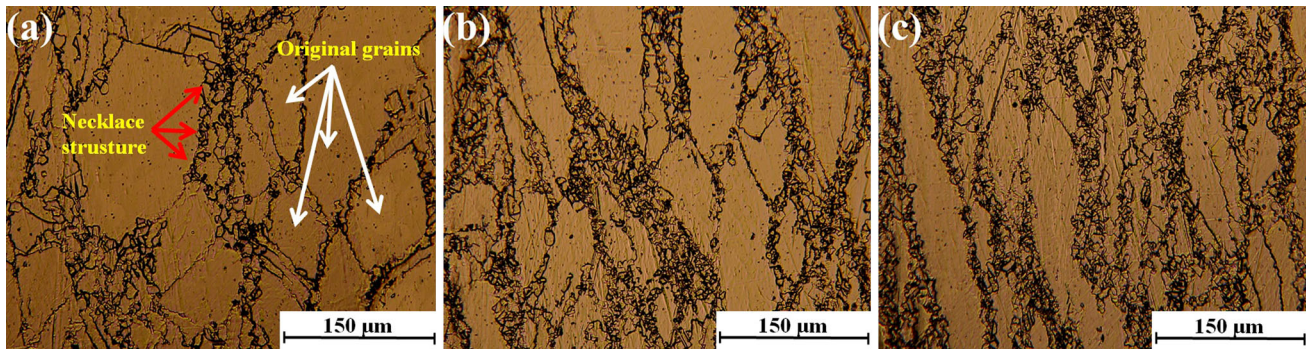


Fig. 6 Optical micrographs of isothermally annealed specimens at 900 °C for (a) 5 min, (b) 10 min and (c) 15 min

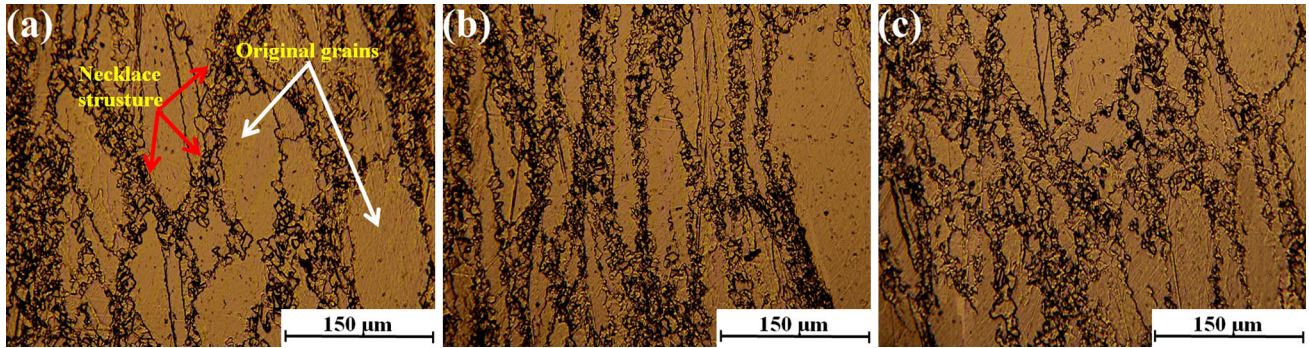


Fig. 7 Optical micrographs of isothermally annealed specimens at 1000 °C for (a) 5 min, (b) 10 min and (c) 15 min

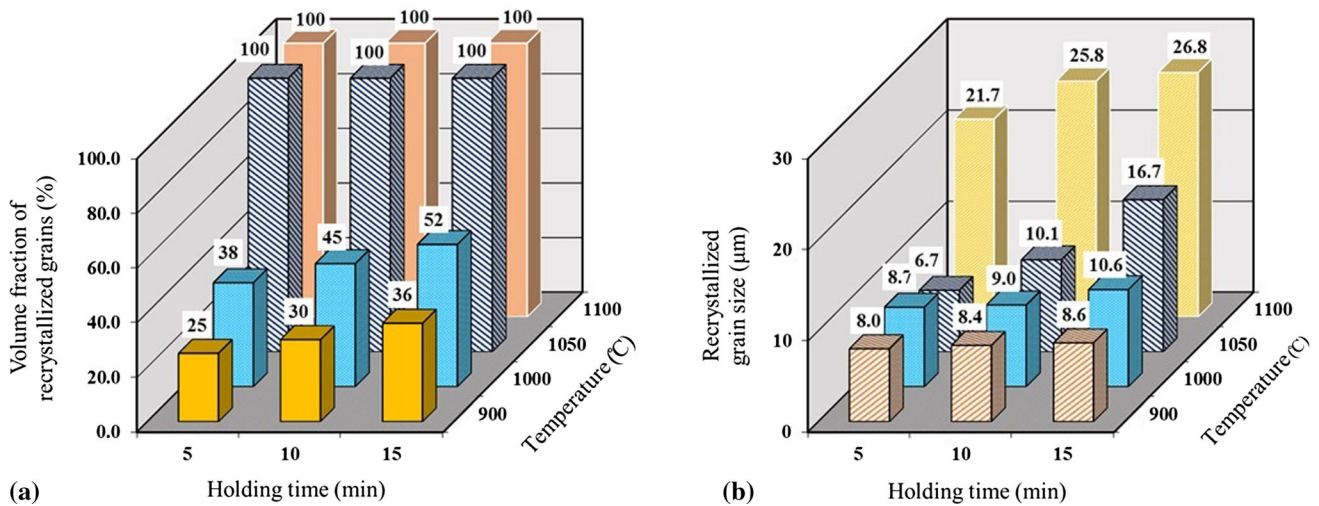


Fig. 8 Variation of the (a) volume fraction of static recrystallized grain and (b) static recrystallized grain size as a function of annealing temperature and holding time

### 3.3 Static Recrystallization Kinetics

In the previous investigation concerning the thermomechanical behavior of steels (Ref 48, 49), the kinetic equation of the static recrystallization has been well developed. The variety of

average recrystallized fraction,  $X_s$ , determined using metallographic observation method, as a function of annealing time, is shown in Fig. 8(a). The static recrystallization kinetics can be described by an Avrami equation of the following form (Ref 50, 51)



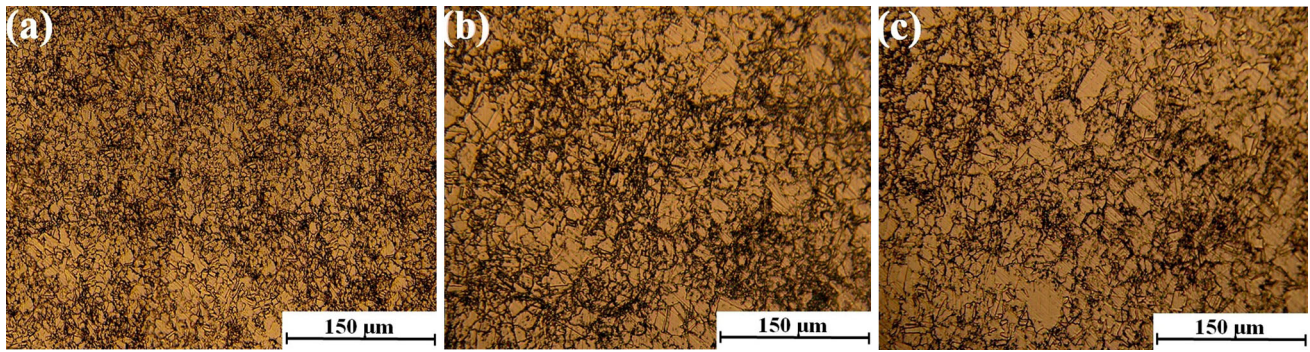


Fig. 9 Optical micrographs of isothermally annealed specimens at 1050 °C for (a) 5 min, (b) 10 min and (c) 15 min

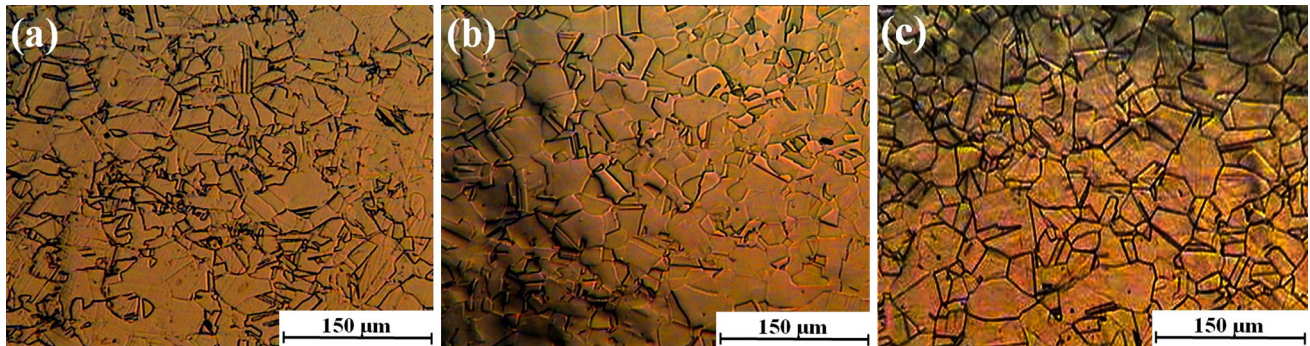


Fig. 10 Optical micrographs of isothermally annealed specimens at 1100 °C for (a) 5 min, (b) 10 min and (c) 15 min

$$X_s = 1 - \exp \left[ -0.693 \left( \frac{t}{t_{0.5}} \right)^n \right] \quad (\text{Eq 2})$$

where  $n$  is the Avrami exponent and  $t_{0.5}$  is the time or responding to 50% recrystallization. It can be defined by the widely used equation (Ref 51):

$$t_{0.5} = A e^p \dot{\epsilon}^q D_0^s \exp \left( \frac{Q}{RT} \right) = B \exp \left( \frac{Q}{RT} \right) \quad (\text{Eq 3})$$

where  $D_0$  is the initial austenitic grain size, which is 132  $\mu\text{m}$  (shown in Fig. 2a) in this research;  $R$  is the gas constant and is equal to 8.314 J/(mol K);  $T$  is the absolute temperature, K;  $Q$  is the apparent activation energy of static recrystallization, J/mol;  $A$ ,  $p$ ,  $q$ ,  $s$  are constants, and the value of  $s$  is generally considered as 1 according to some researches (Ref 49, 52). In this research, all calculations were done at strain rate of 0.1  $\text{s}^{-1}$  and true strain of 0.7 and the initial grain size of 132  $\mu\text{m}$ .

Taking the natural logarithm of Eq 2, the following expression can be obtained:

$$\ln \left[ \ln \left( \frac{1}{1 - X_s} \right) \right] = \ln 0.693 + n \ln t - n \ln t_{0.5} \quad (\text{Eq 4})$$

By plotting  $\ln \left[ \ln \left( \frac{1}{1 - X_s} \right) \right]$  versus  $\ln t$  and linear regression under each deformation condition, the Avrami exponent  $n$  can be determined as shown in Fig. 11(a). The average value of  $n$  under all the deformation conditions can be obtained as 0.38.

Take the natural logarithm of Eq 3,

$$\ln t_{0.5} = \ln B + \frac{Q}{RT} \quad (\text{Eq 5})$$

The relationship between  $\ln t_{0.5}$  and  $1/T$  is linear and  $Q/R$  is the slope. By the linear regression,  $Q/R$  could be obtained as 20.1149 (Fig. 11b). Then  $Q$  can be calculated as 167,235  $\text{J mol}^{-1}$ . The constant of  $B$  can be derived from Eq 5 as 1.78E-06. Then, the static recrystallization kinetics of Sanicro 28 austenitic stainless steel can be described as follows:

$$X_s = 1 - \exp \left[ -0.693 \left( t/t_{0.5} \right)^{0.38} \right] \quad (\text{Eq 6})$$

$$t_{0.5} = 1.78 \times 10^{-6} \exp(167235/RT)$$

### 3.4 Mechanical Properties of Annealed Specimens

Figure 12 illustrates the effects of annealing temperature and holding time on the tensile elongation of the experimental alloy obtained from shear punch testing method. According to the above discussion, the soaking temperature and/or holding time affect static recrystallization, since the microstructural evolution was strongly dependent to the deformation history of the alloy, as well as subsequent heat treatment parameters. In general, it is found that the elongation of processed CRSA steel increases with increasing the annealing temperature and decreases slightly with increasing holding time because of gradually grain growth (Ref 12). By increasing temperature from 1050 to 1100 °C, the grain coarsening brings down the

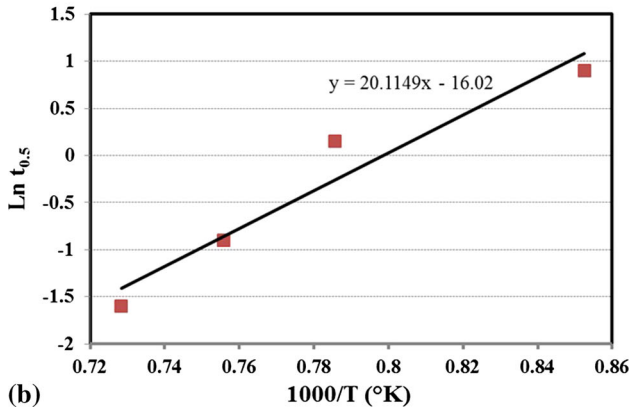
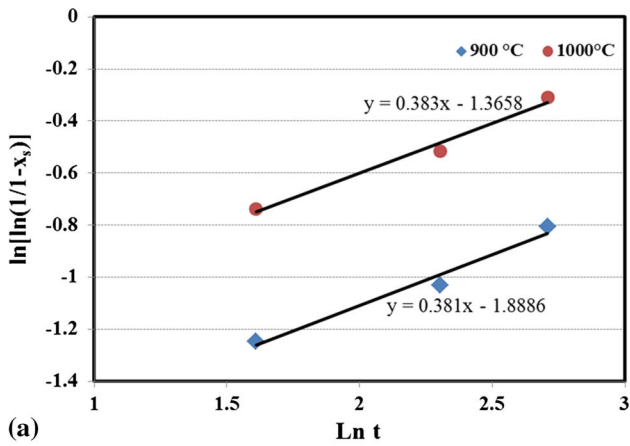


**Fig. 11** (a) Graphical representation of the relationship between the recrystallized fraction and the recrystallization time, (b) plot of the empirical relation  $\ln t_{0.5}$  against the reciprocal of the absolute temperature

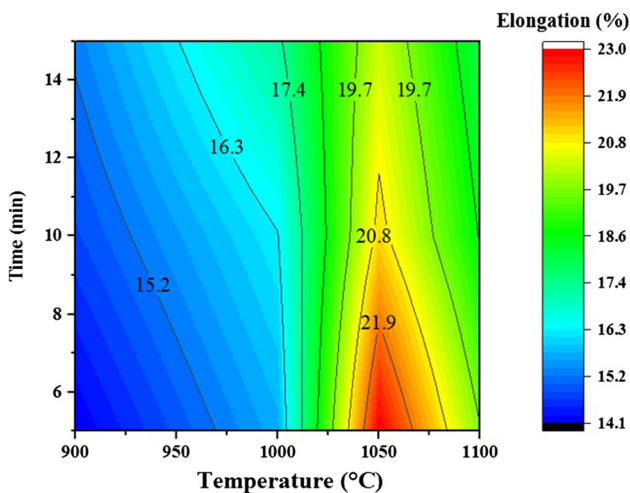


**Fig. 12** Contour mapping represents the amount of elongation after post-annealing

percentage elongation values, as observed in the present work. Therefore, grain growth is the one responsible for the decrease in elongation values.

## 4. Conclusions

The cold work process followed by annealing treatment which produces a structural evolution of restoration and recrystallization is a standard practice for alloys to improve their mechanical properties. Based on investigation results, it was concluded that the post-deformation annealing treatment has a great influence on characteristics of the Sanicro 28 steel. Therefore, the dependency of mechanical properties to annealing conditions at elevate temperatures is of practical importance. Increasing the annealing temperature in the range of 900–1100 °C leads to an increase in volume fraction of the grains which underwent partially static recrystallization. The annealing treatment at 1000 °C leads to the formation of fine-grained structure as a result of recrystallization. Such microstructure shows evident increase in the characteristics of elongation in comparison with annealing at lower temperature. The increase in annealing temperature up to 1050 °C leads to the completely static recrystallized and the further increase in the characteristics of elongation. By increasing temperature up to 1100 °C, the grain coarsening after complete recrystallization occurs at higher temperatures under whole times.

## References

1. A. Zambon, P. Ferro, and F. Bonollo, Microstructural, Compositional and Residual Stress Evaluation of CO<sub>2</sub> Laser Welded Superaustenitic AISI, 904L Stainless Steel, *Mater. Sci. Eng. A*, 2006, **424**(1), p 117–127
2. A. Mirzaei, A. Zarei-Hanzaki, M. Pishbin, A. Imandoust, and S. Khoddam, Evaluating the Hot Deformation Behavior of a Super-Austenitic Steel Through Microstructural and Neural Network Analysis, *J. Mater. Eng. Perform.*, 2015, **24**(6), p 2412–2421
3. K. Mehta, P. Mukhopadhyay, R. Mandal, and A. Singh, Mechanical Properties Anisotropy of Cold Rolled and Solution Annealed Ni-20Cr-8Fe alloy, *Mater. Sci. Eng. A*, 2014, **613**, p 71–81
4. N. Dudova, A. Belyakov, and R. Kaibyshev, Recrystallization Behavior of a Ni-20% Cr Alloy Subjected to Severe Plastic Deformation, *Mater. Sci. Eng. A*, 2012, **543**, p 164–172
5. R.W. Fonda, E. Lauridsen, W. Ludwig, P. Tafforeau, and G. Spanos, Two-Dimensional and Three-Dimensional Analyses of Sigma Precipitates and Porosity in a Superaustenitic Stainless Steel, *Metall. Mater. Trans. A*, 2007, **38**(11), p 2721–2726
6. A. Mirzaei, A. Zarei-Hanzaki, and H. Abedi, Hot Ductility Characterization of Sanicro-28 Super-Austenitic Stainless Steel, *Metall. Mater. Trans. A*, 2016, **47**(5), p 2037–2048
7. A. Mohamadizadeh, A. Zarei-Hanzaki, A. Kisko, and D. Porter, Ultra-Fine Grained Structure Formation Through Deformation-Induced Ferrite Formation in Duplex Low-Density Steel, *Mater. Des.*, 2016, **92**, p 322–329
8. A. Mohamadizadeh, A. Zarei-Hanzaki, H. Abedi, S. Mehtonen, and D. Porter, Hot Deformation Characterization of Duplex Low-Density Steel Through 3D Processing Map Development, *Mater. Charact.*, 2015, **107**, p 293–301
9. C. Donadille, R. Valle, P. Dervin, and R. Penelle, Development of Texture and Microstructure During Cold-Rolling and Annealing of FCC Alloys: Example of an Austenitic Stainless Steel, *Acta Metall.*, 1989, **37**(6), p 1547–1571
10. H. Chao, H. Sun, W. Chen, and E. Wang, Static Recrystallization Kinetics of a Heavily Cold Drawn AZ31 Magnesium Alloy Under Annealing Treatment, *Mater. Charact.*, 2011, **62**(3), p 312–320
11. Y. Lin, Y.-X. Liu, M.-S. Chen, M.-H. Huang, X. Ma, and Z.-L. Long, Study of Static Recrystallization Behavior in Hot Deformed Ni-Based Superalloy Using Cellular Automaton Model, *Mater. Des.*, 2016, **99**, p 107–114



12. V. Torabinejad, A. Zarei-Hanzaki, M. Sabet, and H. Abedi, The Effect of Low Temperature Annealing on the Mechanical Behavior of Cold Rolled Dual-Phase Twinning-Induced Plasticity Steel, *Mater. Des.*, 2011, **32**(4), p 2345–2349
13. G. Mohamed and B. Bacroix, Role of Stored Energy in Static Recrystallization of Cold Rolled Copper Single and Multicrystals, *Acta Mater.*, 2000, **48**(13), p 3295–3302
14. B. Mirzakhani, M.T. Salehi, S. Khoddam, S.H. Seyedein, and M.R. Aboutalebi, Investigation of Dynamic and Static Recrystallization Behavior During Thermomechanical Processing in a API-X70 Microalloyed Steel, *J. Mater. Eng. Perform.*, 2009, **18**(8), p 1029–1034
15. T. Sakai, A. Belyakov, R. Kaibyshev, H. Miura, and J.J. Jonas, Dynamic and Post-dynamic Recrystallization Under Hot, Cold and Severe Plastic Deformation Conditions, *Prog. Mater. Sci.*, 2014, **60**, p 130–207
16. R. Doherty, D. Hughes, F. Humphreys, J. Jonas, D.J. Jensen, M. Kassner, W. King, T. McNelley, H. McQueen, and A. Rollett, Current Issues in Recrystallization: A Review, *Mater. Sci. Eng. A*, 1997, **238**(2), p 219–274
17. X.-M. Chen, Y. Lin, M.-S. Chen, H.-B. Li, D.-X. Wen, J.-L. Zhang, and M. He, Microstructural Evolution of a Nickel-Based Superalloy During Hot Deformation, *Mater. Des.*, 2015, **77**, p 41–49
18. H. Miura, T. Sakai, A. Belyakov, G. Gottstein, M. Crumbach, and J. Verhasselt, Static Recrystallization of SiO<sub>2</sub>-Particle Containing {011} <100> Copper Single Crystals, *Acta Mater.*, 2003, **51**(6), p 1507–1515
19. H. Ahlborn, E. Hornbogen, and U. Köster, Recrystallisation Mechanism and Annealing Texture in Aluminium-Copper Alloys, *J. Mater. Sci.*, 1969, **4**(11), p 944–950
20. Y. Lin, X.-Y. Wu, X.-M. Chen, J. Chen, D.-X. Wen, J.-L. Zhang, and L.-T. Li, EBSD Study of a Hot Deformed Nickel-Based Superalloy, *J. Alloys Compd.*, 2015, **640**, p 101–113
21. I. Gutierrez-Urrutia and D. Raabe, Dislocation and Twin Substructure Evolution During Strain Hardening of an Fe-22wt.% Mn–0.6 wt.% C TWIP Steel Observed by Electron Channeling Contrast Imaging, *Acta Mater.*, 2011, **59**(16), p 6449–6462
22. X. Li, J. Zhang, L. Rong, and Y. Li, Effect of Twins on the Moderate Temperature Tensile Deformation of a  $\gamma'$  Strengthened Fe-Based Superalloy, *J. Alloys Compd.*, 2009, **467**(1), p 383–389
23. D. Bhattacharyya, E. Cerreta, R. McCabe, M. Niewczas, G. Gray, A. Misra, and C. Tome, Origin of Dislocations Within Tensile and Compressive Twins in Pure Textured Zr, *Acta Mater.*, 2009, **57**(2), p 305–315
24. K. Rahman, V. Vorontsov, and D. Dye, The Effect of Grain Size on the Twin Initiation Stress in a TWIP Steel, *Acta Mater.*, 2015, **89**, p 247–257
25. J. Kacher and A.M. Minor, Twin Boundary Interactions with Grain Boundaries Investigated in Pure Rhenium, *Acta Mater.*, 2014, **81**, p 1–8
26. L. Remy, Twin–Slip Interaction in fcc Crystals, *Acta Metall.*, 1977, **25**(6), p 711–714
27. L. Remy, The Interaction Between Slip and Twinning Systems and the Influence of Twinning on the Mechanical Behavior of fcc Metals and Alloys, *Metall. Trans. A*, 1981, **12**(3), p 387–408
28. A.F. Padilha, R.L. Plaut, and P.R. Rios, Annealing of Cold-Worked Austenitic Stainless Steels, *ISIJ Int.*, 2003, **43**(2), p 135–143
29. S.-H. Wang, Z.-Y. Liu, G.-D. Wang, J.-L. Liu, G.-F. Liang, and Q.-L. Li, Effects of Twin-Dislocation and Twin–Twin Interactions on the Strain Hardening Behavior of TWIP Steels, *J. Iron. Steel Res. Int.*, 2010, **17**(12), p 70–74
30. F.J. Humphreys and M. Hatherly, *Recrystallization and Related Annealing Phenomena*, 2nd ed., Pergamon, Dordrecht, 2004
31. A. Mirzaei, A. Zarei-Hanzaki, N. Haghdadi, and A. Marandi, Constitutive Description of High Temperature Flow Behavior of Sanicro-28 Super-Austenitic Stainless Steel, *Mater. Sci. Eng. A*, 2014, **589**, p 76–82
32. V. Kain, K. Chandra, K. Adhe, and P. De, Effect of Cold Work on Low-Temperature Sensitization Behaviour of Austenitic Stainless Steels, *J. Nucl. Mater.*, 2004, **334**(2), p 115–132
33. D. Barraclough and C. Sellars, Static Recrystallization and Restoration After Hot Deformation of Type 304 Stainless Steel, *Met. Sci.*, 1979, **13**(3–4), p 257–268
34. M. Eskandari, A. Zarei-Hanzaki, and H.R. Abedi, An Investigation into the Room Temperature Mechanical Properties of Nanocrystalline Austenitic Stainless Steels, *Mater. Des.*, 2013, **45**, p 674–681
35. A. Behravan, A. Zarei-Hanzaki, M. Ghambari, M. Moallemi, and A. Mohamadizadeh, Correlation Between Warm Deformation Characteristics and Mechanical Properties of a New TRIP-Assisted Fe-MN-Ni Steel, *Mater. Sci. Eng. A*, 2016, **649**, p 27–34
36. M. Moallemi, A. Zarei-Hanzaki, and A. Mirzaei, On the Stacking Fault Energy Evaluation and Deformation Mechanism of Sanicro-28 Super-Austenitic Stainless Steel, *J. Mater. Eng. Perform.*, 2015, **24**(6), p 2335–2340
37. B. Hutchinson and N. Ridley, On Dislocation Accumulation and Work Hardening in Hadfield Steel, *Scr. Mater.*, 2006, **55**(4), p 299–302
38. J.W. Christian and S. Mahajan, Deformation Twinning, *Prog. Mater. Sci.*, 1995, **39**(1–2), p 1–157
39. C.A. Bronkhorst, S.R. Kalidindi, and L. Anand, Polycrystalline Plasticity and the Evolution of Crystallographic Texture in FCC Metals, *Philos. Trans. R. Soc. Lond. A Math. Phys. Eng. Sci.*, 1992, **341**(1662), p 443–477
40. S. Panchanadeeswaran, R. Doherty, and R. Becker, Direct Observation of Orientation Change by Channel Die Compression of Polycrystalline Aluminum—Use of a Split Sample, *Acta Mater.*, 1996, **44**(3), p 1233–1262
41. L. Remy, Kinetics of fcc Deformation Twinning and Its Relationship to Stress-Strain Behaviour, *Acta Metall.*, 1978, **26**(3), p 443–451
42. H. Abedi, A.Z. Hanzaki, N. Haghdadi, and P. Hodgson, Substructure Induced Twinning in Low Density Steel, *Scr. Mater.*, 2017, **128**, p 69–73
43. S. Mahajan and G. Chin, The Interaction of Twins With Existing Substructure and Twins in Cobalt-Iron Alloys, *Acta Metall.*, 1974, **22**(9), p 1113–1119
44. S. Mahajan and G. Chin, Twin–Slip, Twin–Twin and Slip–Twin Interactions in Co-8 wt.% Fe Alloy Single Crystals, *Acta Metall.*, 1973, **21**(2), p 173–179
45. O. Kwon and A. DeArdo, Interactions Between Recrystallization and Precipitation in Hot-Deformed Microalloyed Steels, *Acta Metall. Mater.*, 1991, **39**(4), p 529–538
46. A. Takayama, X. Yang, H. Miura, and T. Sakai, Continuous Static Recrystallization in Ultrafine-Grained Copper Processed by Multi-directional Forging, *Mater. Sci. Eng. A*, 2008, **478**(1), p 221–228
47. C. Schäfer, V. Mohles, and G. Gottstein, Modeling of Non-Isothermal Annealing: Interaction of Recrystallization, Recovery, and Precipitation, *Acta Mater.*, 2011, **59**(17), p 6574–6587
48. Y. Lin, M.-S. Chen, and J. Zhong, Study of Static Recrystallization Kinetics in a Low Alloy Steel, *Comput. Mater. Sci.*, 2008, **44**(2), p 316–321
49. J. Miao, L. Bo, X.-g. Liu, G. Huan, H.-p. Ji, and B.-f. Guo, Static Recrystallization Behavior of 316LN Austenitic Stainless Steel, *J. Iron. Steel Res. Int.*, 2013, **20**(11), p 67–72
50. E. Am, E. Essadiqi, and S. Yue, The Kinetics of Static Recrystallization in Microalloyed Hypereutectoid Steels, *ISIJ Int.*, 2004, **44**(1), p 162–170
51. Z.-X. Xie, H.-Y. Gao, W. Jun, Y. Yan, F. Yuan, and B.-D. Sun, Static Recrystallization Behavior of Twin Roll Cast Low-Carbon Steel Strip, *J. Iron. Steel Res. Int.*, 2011, **18**(2), p 45–51
52. S.-H. Cho and Y.-C. Yoo, Static Recrystallization Kinetics of 304 Stainless Steels, *J. Mater. Sci.*, 2001, **36**(17), p 4273–4278